

The connection between stellar mass, age and quenching timescale in massive quiescent galaxies at $z \simeq 1$

M. L. Hamadouche^{1*}, A. C. Carnall¹, R. J. McLure¹, J. S. Dunlop¹, R. Begley¹, F. Cullen¹
D. J. McLeod¹, C. T. Donnan¹ and T. M. Stanton¹

¹*SUPA[†], Institute for Astronomy, University of Edinburgh, Royal Observatory, Edinburgh, EH9 3HJ, UK*

Accepted XXX. Received YYY; in original form ZZZ

ABSTRACT

We present a spectro-photometric study of a mass-complete sample of quiescent galaxies at $1.0 < z < 1.3$ with $\log_{10}(M_*/M_\odot) \geq 10.3$ drawn from the VANDELS survey, exploring the relationship between stellar mass, age and star-formation history. Within our sample of 114 galaxies, we derive a stellar-mass vs stellar-age relation with a slope of $1.20^{+0.28}_{-0.27}$ Gyr per decade in stellar mass. When combined with recent literature results, we find evidence that the slope of this relation remains consistent over the redshift interval $0 < z < 4$. The galaxies within the VANDELS quiescent sample display a wide range of star-formation histories, with a mean star-formation timescale of 1.5 ± 0.1 Gyr and a mean quenching timescale of 1.4 ± 0.1 Gyr. We then focus on the oldest galaxies in our sample, finding that the number density of galaxies that quenched before $z = 3$ with stellar masses $\log_{10}(M_*/M_\odot) \geq 10.6$ is $(1.1 \pm 0.7) \times 10^{-5} \text{ Mpc}^{-3}$. Although uncertain, this estimate is in good agreement with the latest observational results at $3 < z < 4$, suggesting that neither rejuvenation nor merger events are playing a major role in the evolution of the oldest massive quiescent galaxies within the redshift interval $1 < z < 3$. Finally, we identify a sub-sample of quiescent galaxies with enhanced CN absorption at $\lambda = 3860 \text{ \AA}$, a feature that has been associated with α -enhancement. Interestingly, this sub-sample exhibits older ages, higher stellar masses and shorter star-formation timescales than the rest of the sample, consistent with expectations for α -enhancement. However, to conclusively link the enhanced CN absorption with α -enhancement will require additional deep near-IR (i.e., rest-frame optical) spectroscopy.

Key words: galaxies: evolution – galaxies: star formation – galaxies: high-redshift

1 INTRODUCTION

It is now well established that the local galaxy population is bi-modal in terms of colour, morphology and star-formation rate (SFR). The colour bi-modality was first observed using data from the Sloan Digital Sky Survey (SDSS, York et al. 2000), with galaxies falling into two categories: a star-forming ‘blue cloud’ and a quiescent ‘red sequence’ (e.g. Strateva et al. 2001; Baldry et al. 2004). In general, more-massive galaxies tend to be red spheroids with little ongoing star formation, whilst less-massive galaxies are mainly blue, star-forming discs. Over the past few decades, many studies have aimed to quantify the mechanisms responsible for producing the bi-modality in the galaxy population (e.g. Dekel & Birnboim 2006; Peng et al. 2010; Gabor & Davé 2012; Schawinski et al. 2014). However, despite the wealth of ground-based and space-based data available, understanding exactly how the shutting down of star formation relates to this distinction between galaxy types remains hugely challenging.

Observations have shown that, even within the quiescent population, galaxies demonstrate a range of characteristics. For example, more-massive galaxies are known to have formed earlier in cosmic time and much more rapidly, with clear evidence for younger stellar populations in less-massive galaxies compared to their more-massive counterparts (e.g. Cowie et al. 1996; Thomas et al. 2005b; Fontana et al. 2006; Fontanot et al. 2009; Pacifici et al. 2016). This phenomenon, referred to as ‘downsizing’, is commonly used to describe the relationship between quiescent galaxy stellar mass and age, and indicates that quenching varies as a function of stellar mass and redshift. Empirical spectral age indicators have provided strong constraints on this downsizing trend, with features such as the D_n4000 index demonstrating positive correlations with stellar mass at redshift, $z \lesssim 1$ (e.g. Bruzual 1983; Balogh et al. 1999; Kauffmann et al. 2003; Brinchmann et al. 2004; Moresco et al. 2011, 2010, 2016).

In addition to the bi-modality of the galaxy population, one of the most important observational results of the past few decades is the differing evolution of the star-forming and quiescent galaxy stellar mass functions (GSMF) across cosmic time, with the number density of quiescent galaxies apparently increasing by almost an order of magnitude since $z \simeq 2$

* E-mail: mham@roe.ac.uk (MLH)

[†] Scottish Universities Physics Alliance

(e.g. Cimatti et al. 2002; Abraham et al. 2004; Baldry et al. 2012; Muzzin et al. 2013; Davidzon et al. 2017; McLeod et al. 2021). However, recent studies also point to a substantial population of massive quiescent galaxies out to $z > 3$ (e.g. Schreiber et al. 2018; Valentino et al. 2020; Carnall et al. 2020, 2022a). Together, these results allow us to quantify the quiescent galaxy fraction across cosmic time, an important observational constraint on galaxy evolution models (e.g., Somerville & Davé 2015).

Another key result was the discovery that the sizes of quiescent galaxies have evolved much more rapidly than their star-forming counterparts since $z \sim 2$, and that quiescent galaxies follow a steeper stellar mass-size relation than star-forming galaxies at all redshifts (e.g. Shen et al. 2003; Trujillo et al. 2006; McLure et al. 2013; van der Wel et al. 2014; Mowla et al. 2019). The physical processes driving the size growth of quiescent galaxies are still not fully understood, although it is widely accepted that minor mergers play an important role in explaining the observed growth from $z \sim 2$ to the local Universe (e.g. see Hopkins et al. 2010; Trujillo et al. 2011; Cimatti et al. 2012; Ownsworth et al. 2014).

Considerable effort has been devoted to understanding which physical mechanisms are required to explain the observed differences in the properties of the star-forming and quiescent galaxy populations. Our understanding of quenching mechanisms relies heavily on simulations of galaxy formation. At $z < 2$, simulations have been able to reproduce the observed bi-modality (see Davé et al. 2017, 2019; Nelson et al. 2018; Akits et al. 2022). However, the situation becomes more complicated at higher redshifts, and it is much more difficult to identify the key physical drivers of quenching. The main mechanisms thought to cause quenching can be categorised into two distinct pathways: ‘mass’ (or ‘internal’, see Somerville & Davé 2015) quenching, and ‘environmental’ quenching. Locally, these two pathways are clearly distinguishable, suggesting that multiple mechanisms quench galaxies (e.g., Peng et al. 2010).

Mass quenching is often thought to be associated with feedback processes such as radiative- or jet-mode active galactic nucleus (AGN) feedback (e.g. Croton et al. 2006; Gabor et al. 2011; Choi et al. 2018). Quenching attributed to galaxy-galaxy interactions (often referred to as ‘environmental’ or ‘satellite’ quenching) is thought to be the result of ram-pressure stripping, caused by satellite galaxies falling into larger dark matter halos, or virial shock-heating of the circum-galactic medium (see Dekel & Birnboim 2006, also referred to as ‘halo’ quenching).

These mechanisms can be further categorised as ‘slow’ and ‘fast’ quenching pathways, respectively (Schawinski et al. 2014; Schreiber et al. 2016; Carnall et al. 2018; Belli et al. 2019). Shorter quenching timescales are thought to be linked with quasar-mode AGN feedback, which is thought to be more prevalent at high redshift (Wild et al. 2016). In contrast, it appears that the key process responsible for quenching at low redshift is the halting of gas accretion, taking place on much longer timescales of several Gyr (e.g. Peng et al. 2015; Trussler et al. 2020).

Large spectroscopic surveys have facilitated increasingly sophisticated, statistical studies of galaxy physical properties at high redshift, with the aim of placing tighter constraints on the physical origins of quenching. The recently completed LEGA-C (van der Wel et al. 2016) and VANDELS (McLure

et al. 2018) surveys provide ultra-deep spectroscopy for hundreds of quiescent galaxies at $0.6 < z < 2.5$. These data sets, coupled with improved spectral energy distribution (SED) fitting methods (e.g. Carnall et al. 2019b; Leja et al. 2019a), have already enabled more-precise measurements of galaxy stellar masses, star-formation histories (SFHs) and stellar metallicities, unveiling significant correlations between these physical properties (e.g. Wu et al. 2018, 2021; Beverage et al. 2021; Carnall et al. 2022b).

A key emerging result is the finding that the observed stellar mass vs stellar age relationship for $z \sim 1$ quiescent galaxies is steeper than is predicted by the most recent generation of cosmological simulations (e.g. Carnall et al. 2019a; Tacchella et al. 2022). These new spectroscopic analyses build upon a corpus of earlier work aiming to quantify these relationships, much of which was founded upon the use of elemental abundances as empirical proxies for formation and quenching timescales (e.g. Thomas et al. 2005a; Conroy et al. 2014; Kriek et al. 2019). Despite these advances in the field, continued, in-depth investigation into the physical properties of quiescent galaxies is still needed to build a thorough understanding of quenching and passive galaxy evolution.

In Hamadouche et al. (2022), we investigated the links between stellar mass, age, size and metallicity using quiescent-galaxy samples from the LEGA-C (van der Wel et al. 2016) and VANDELS (McLure et al. 2018) spectroscopic surveys at $z \simeq 0.7$ and $z \simeq 1.1$, respectively. We examined stellar mass-age trends using the D_n4000 index as a proxy for the stellar population age, finding that more-massive galaxies exhibit higher D_n4000 values at both redshift ranges, consistent with prior evidence for the downsizing scenario at lower redshifts. In this work, we return to the VANDELS spectroscopic sample, building upon our previous results by employing full spectral fitting to probe the ages and SFHs of massive quiescent galaxies at $z \gtrsim 1$ in detail.

This study makes use of the fully completed VANDELS DR4 sample (Garilli et al. 2021), which includes more than twice the number of quiescent galaxy spectra studied in the initial analysis of Carnall et al. (2019a). Moreover, in this study we implement an improved physical model, along with additional metallicity constraints for the VANDELS sample from Carnall et al. (2022b), to better constrain star-formation histories, stellar masses and formation and quenching times. Motivated by the ongoing challenges in quantifying the correlations between key quiescent galaxy physical properties, we begin by examining the relationship between stellar mass and age in our quiescent sample at $1.0 < z < 1.3$, and discuss these results in the context of downsizing. We then explore the typical quenching timescales of $z \sim 1$ quiescent galaxies, focusing on a sub-sample of galaxies that display spectral features associated with α -enhancement.

The structure of this paper is as follows. We introduce the VANDELS survey in Section 2, before providing details of our sample selection and spectral fitting technique using the BAGPIPES code (Carnall et al. 2018) in Section 3. We present our main results in Section 4 and discuss them in Section 5. Finally, we present our conclusions in Section 6. Throughout this paper, we assume a Kroupa (2001) initial mass function and the Asplund et al. (2009) Solar abundance of $Z_\odot = 0.0142$. We assume cosmological parameters $H_0 = 70 \text{ km s}^{-1} \text{ Mpc}^{-1}$, $\Omega_m = 0.3$ and $\Omega_\Lambda = 0.7$ throughout. All magnitudes are quoted in the AB system.

2 THE VANDELS SURVEY

VANDELS is a large ESO Public Spectroscopy Survey (McLure et al. 2018; Pentericci et al. 2018; Garilli et al. 2021) targeting the CDFS and UDS fields, and covering a total area of 0.2 deg^2 . The survey data were obtained using the Visible Multi-Object Spectrograph (VIMOS, Le Fèvre et al. 2004) on the ESO VLT. The final data release (DR4; Garilli et al. 2021) provides spectra for a sample of 2087 galaxies, the vast majority of which (87 per cent) are star-forming galaxies in the redshift range $2.4 < z < 6.2$. However, in this study, we focus on the remaining 281 targets (13 per cent) selected as quiescent galaxies in the redshift range $1.0 < z < 2.5$.

2.1 VANDELS sample selection

The VANDELS spectroscopic sample was originally drawn from a combination of four separate photometric catalogues. Two of these are the CANDELS GOODS South and UDS catalogues (Guo et al. 2013; Galametz et al. 2013), whilst the other two are custom ground-based catalogues (described in McLure et al. 2018), covering the wider VANDELS area outside of the CANDELS footprints.

The parent quiescent sample was selected from these photometric catalogues as follows. Objects were required to have H -band magnitudes of $H \leq 22.5$, corresponding to stellar masses of $\log_{10}(M_*/M_\odot) \gtrsim 10$, as well as i -band magnitudes of $i \leq 25$. To separate star-forming and quiescent galaxies, rest-frame UVJ criteria were applied following Williams et al. (2009). These criteria result in a sample of 812 galaxies, which we refer to as the VANDELS photometric parent sample.

2.2 VANDELS spectroscopy

Here we briefly summarise the VANDELS spectroscopic observations, while referring the reader to Pentericci et al. (2018) for a full description. From the parent sample of 812 quiescent galaxies described in the previous section, 281 were randomly assigned slits and observed as part of the VANDELS survey. Objects were observed for 20, 40 or 80 hours depending on their i -band magnitudes. The observations were obtained using the MR grism, providing a median resolution of $R \sim 600$ across a wavelength range from $\lambda = 4800\text{--}9800 \text{ \AA}$. The VANDELS team manually measured spectroscopic redshifts, assigning redshift quality flags according to Le Fèvre et al. (2013). In this paper we only use those galaxies with spectroscopic redshift flag 3 or 4, which has subsequently been shown to correspond to a $\simeq 99$ per cent probability of being correct (Garilli et al. 2021).

3 METHODOLOGY AND SAMPLE SELECTION

The VANDELS observations described in Section 2 produce an initial sample of 269 quiescent galaxies with robust spectroscopic redshifts, of which 87 per cent have $1 < z_{\text{spec}} < 1.5$. In this section, we describe the selection of the final quiescent sample that we use for our analysis.

3.1 Spectro-photometric fitting

We use BAGPIPES (Carnall et al. 2018) to simultaneously fit the available spectroscopic and photometric data for our initial sample of 269 quiescent galaxies. We incorporate several improvements to the model used to fit the VANDELS photometric catalogues in Hamadouche et al. (2022) (based on Carnall et al. 2019a), which we briefly describe below.

We use a double-power-law star-formation history model, employing the updated 2016 versions of the BC03 stellar population synthesis models (Bruzual & Charlot 2003; Chevalard & Charlot 2016). We also vary the stellar metallicity from $Z_* = 0.2 - 2.5Z_\odot$ using a logarithmic prior. We use the Salim et al. (2018) dust attenuation law, which parameterises the dust-curve shape through a power-law deviation, δ , from the Calzetti et al. (2000) law. Nebular continuum and emission lines are modelled using the CLOUDY photoionization code (Ferland et al. 2017), using a method based on that of Byler et al. (2017). We assume a fixed ionization parameter of $\log_{10}(U) = -3$. Full details of the free parameters and priors used in our fitting are provided in Table 1.

We take into account systematic uncertainties in the observed spectra of our galaxies by applying additive noise and multiplicative calibration models (e.g., van der Wel et al. 2016; Cappellari 2017; Johnson et al. 2021). We follow the approach outlined in Section 4 of Carnall et al. (2019a), by fitting a second-order multiplicative Chebyshev polynomial to account for problems with flux calibration, and an additive Gaussian process model with an exponential squared kernel to model correlated additive noise between spectral pixels in our data.

3.2 A mass-complete sample

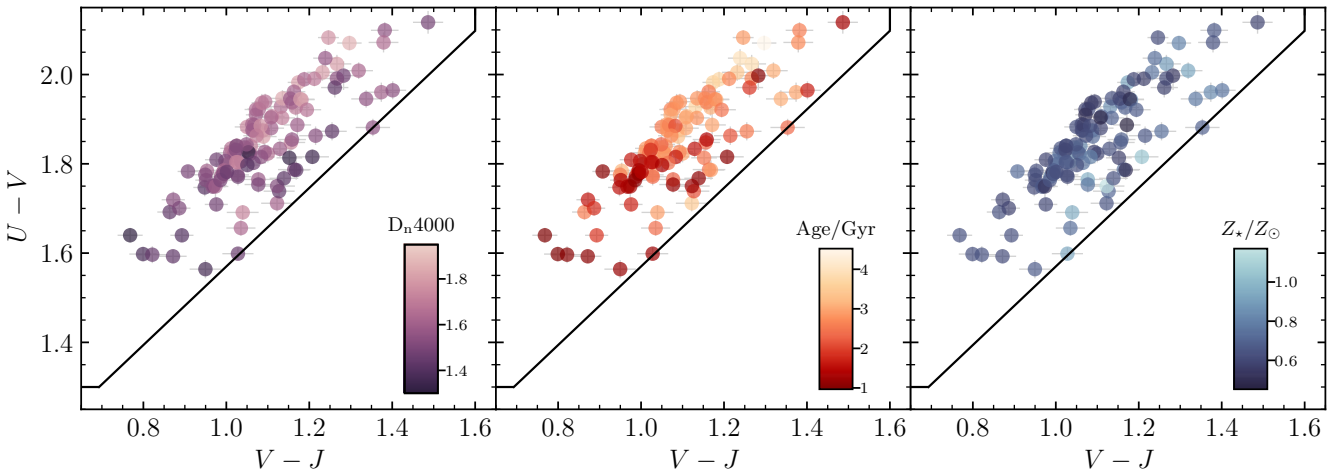
To ensure that our final sample is mass complete, we restrict the sample to $\log_{10}(M_*/M_\odot) \geq 10.3$ and $1.0 \leq z \leq 1.3$ (see Carnall et al. 2019a). In addition, we require members of the sample to have $U - V > 0.88 \times (V - J) + 0.69$, in order to remove green-valley galaxies. This has been shown to be broadly equivalent to a specific SFR cut of $\text{sSFR} < 0.2/t_H$, where t_H is the age of the Universe at the relevant redshift (Carnall et al. 2018). These criteria produce a sample of 139 quiescent galaxies.

To clean the quiescent sample of potential X-ray contaminants, we remove five objects with matches in either the *Chandra* Seven Mega-second catalogue (Luo et al. 2017) or the X-UDS catalogue (Kocevski et al. 2018) that cover the CDFS and UDS fields, respectively. All five galaxies with X-ray matches also display strong [OII] emission in their rest-frame UV spectra. We also search for potential radio-loud AGN using the Very Large Array (VLA) 1.4 GHz data available for both fields (Simpson et al. 2006; Bonzini et al. 2013), finding one additional AGN candidate. This object was not removed from the quiescent sample because it does not display strong [OII] emission.

Finally, we remove one galaxy whose spectrum is highly contaminated (due to a nearby object), leaving a final, cleaned sample of 114 quiescent VANDELS galaxies. This final sample is shown on the UVJ plane in Fig. 1, colour-coded by mass-weighted age, D_n4000 and stellar metallicity.

Table 1. Details of the parameter ranges and priors adopted for the BAGPIPES fitting of the VANDELS photometry and spectroscopy (see Section 3.1). Priors listed as logarithmic are uniform in log-base-ten of the parameter.

Component	Parameter	Symbol / Unit	Range	Prior	Hyperparameters
Global	Redshift	z_{spec}	$z_{\text{spec}} \pm 0.015$	Gaussian	$\mu = z_{\text{spec}} \sigma = 0.005$
SFH	Stellar mass formed	M_*/M_\odot	$(1, 10^{13})$	log	
	Metallicity	Z_*/Z_\odot	$(0.2, 2.5)$	log	
	Falling slope	α	$(0.1, 10^3)$	log	
	Rising slope	β	$(0.1, 10^3)$	log	
	Peak time	τ/Gyr	$(0.1, t_{\text{obs}})$	uniform	
Dust	Attenuation at 5500 Å	A_V/mag	$(0, 4)$	uniform	
	Deviation from Calzetti et al. (2000) slope	δ	$(-0.3, 0.3)$	Gaussian	$\mu = 0.0, \sigma = 0.1$
	Strength of 2175 Å bump	B	$(0, 5)$	uniform	
Calibration	Zeroth order	P_0	$(0.5, 1.5)$	Gaussian	$\mu = 1.0, \sigma = 0.25$
	First order	P_1	$(-0.5, 0.5)$	Gaussian	$\mu = 0.0, \sigma = 0.25$
	Second order	P_2	$(-0.5, 0.5)$	Gaussian	$\mu = 0.0, \sigma = 0.25$
Noise	White-noise scaling	a	$(0.1, 10)$	log	
	Correlated noise amplitude	b/f_{max}	$(0.0001, 1)$	log	
	Correlation length	$l/\Delta\lambda$	$(0.01, 1)$	log	

**Figure 1.** The distribution of the final mass-complete sample of 114 quiescent VANDELS galaxies on the UVJ plane, highlighting trends between the rest-frame UVJ colours and (left to right) D_n4000 , mass-weighted age and stellar metallicity. The first two panels show that redder rest-frame UVJ colours correlate with higher D_n4000 values and older mass-weighted ages, consistent with literature results (e.g., Belli et al. 2019; Carnall et al. 2019a). The last panel, colour-coded by metallicity, does not demonstrate any significant trend.

3.3 Stacked spectra

In the sections of our analysis where we make use of stacked spectra, we use the following standard procedure to produce our stacks. We first de-redshift and then re-sample each individual spectrum onto a uniform 2.5 Å wavelength grid using the spectral re-sampling module SPECTRES (Carnall 2017). Prior to stacking, we normalise by the median flux across the wavelength range $3500 - 3700 \text{ Å}$. The median flux across all spectra in each pixel is then calculated. Uncertainties in the stacked spectra are calculated using the standard error on the median.

For stacked spectra where we wish to show correlations with D_n4000 , the spectrum is then normalised by the median flux in the blue continuum band of the D_n4000 index,

such that the median flux density in the red continuum band corresponds to the D_n4000 index of the stacked spectrum. We calculate D_n4000 using the same prescription outlined in Section 3.4 of Hamadouche et al. (2022).

3.4 Size measurements

We use the GALFIT (Peng et al. 2002) size measurements from Hamadouche et al. (2022) for 110/114 galaxies in the final sample. For the remaining galaxies we adopted an identical procedure to Hamadouche et al. (2022), using *HST* F160W images for the three galaxies within the CANDELS footprint and *HST* ACS F850LP imaging in CDFS for the single galaxy lying outside the CANDELS footprint.

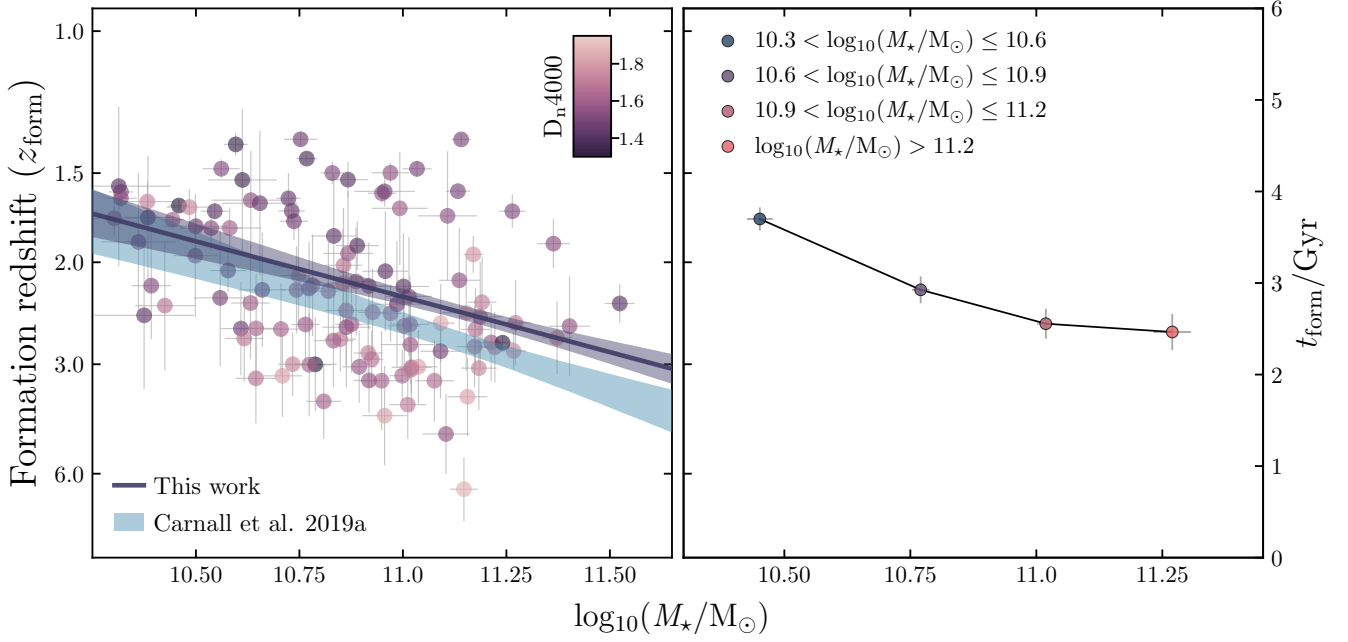


Figure 2. *Left:* Stellar mass versus formation redshift for our final mass-complete VANDELS DR4 quiescent galaxy sample. The sample is colour-coded by D_{n4000} , demonstrating a clear preference for higher D_{n4000} values at earlier formation times. The relationship we fit in Section 4.2 is shown in purple, with the 1σ confidence interval shaded. The relation derived for a smaller sample from VANDELS DR2 by Carnall et al. (2019a) is shown in blue. *Right:* Median formation redshifts for our sample in 0.3-dex bins. The error bars are the standard errors for $t_{\text{form}}/\text{Gyr}$ and $\log_{10}(M_*/M_\odot)$ in each stellar-mass bin. A clear negative correlation is observed. The final bin contains only ten objects above $\log_{10}(M_*/M_\odot) > 11.2$, meaning that the apparent flattening of the relationship is challenging to assess.

4 RESULTS

In this section, we present the results obtained from full-spectral fitting of our final quiescent galaxy sample.

4.1 Trends with rest-frame UVJ colour

In Fig. 1, we show the distribution of the final mass-complete sample of VANDELS quiescent galaxies (see Section 3.2) on the rest-frame UVJ diagram, coloured by mass-weighted age, D_{n4000} , and stellar metallicity. In the first panel, we see that the galaxies with redder $U-V$ and $V-J$ colours, also tend to have higher mass-weighted ages, consistent with recent literature results (e.g., Belli et al. 2019; Carnall et al. 2019a). In the next panel, the trend with D_{n4000} is similar; lighter-coloured points indicate higher D_{n4000} values, which is consistent with the trend seen in other samples at similar redshifts (e.g. Whitaker et al. 2013). The final panel of Fig. 1 shows the sample coloured by metallicity. There is no obvious trend between metallicity and UVJ colour. The individual metallicities we measure are however consistent with scattering around the median value of $\log_{10}(Z_*/Z_\odot) = -0.13 \pm 0.08$ determined from an optical+NIR stack at $z \sim 1.15$ by Carnall et al. (2022b).

4.2 The relationship between stellar mass and age

We present our results for the stellar-mass vs age relation in Fig. 2. We plot redshift of formation, z_{form} , against stellar

mass. The right-hand axis shows the corresponding formation time, t_{form} , measured forwards from the Big Bang. In this paper, we take t_{form} and z_{form} to be the age of the Universe and redshift corresponding to the mass-weighted age of the galaxy. We see a clear negative correlation, albeit with considerable scatter. A trend is also visible between t_{form} and D_{n4000} in Fig. 2, with galaxies that have earlier formation times exhibiting higher values of D_{n4000} , as would be expected.

We fit a linear relationship between t_{form} and $\log_{10}(M_*/M_\odot)$, including an intrinsic scatter term, using the nested sampling Monte Carlo algorithm MLFriends (Buchner 2016, 2019) using the UltraNest¹ package (Buchner 2021). We derive a best-fitting relation of:

$$(t_{\text{form}} / \text{Gyr}) = 2.85^{+0.08}_{-0.09} - 1.20^{+0.28}_{-0.27} \log_{10}(M_*/10^{11} M_\odot). \quad (1)$$

We also find an intrinsic scatter of $(t_{\text{form}} / \text{Gyr}) = 0.51^{+0.09}_{-0.07}$. We show the fit to our data in Fig. 2 (purple line) with the shaded region showing the 1σ confidence interval.

We also show the result derived by Carnall et al. (2019a), using the VANDELS DR2 sample of 53 galaxies, which is a subset of our new 114-galaxy final VANDELS sample. The slope of our new relation is in good agreement with this previous result, however we recover a ~ 300 Myr offset towards younger ages.

To explore the origin of this offset, we re-fit our linear model to the sub-sample of 53 galaxies used by Carnall et al.

¹ <https://johannesbuchner.github.io/UltraNest/>

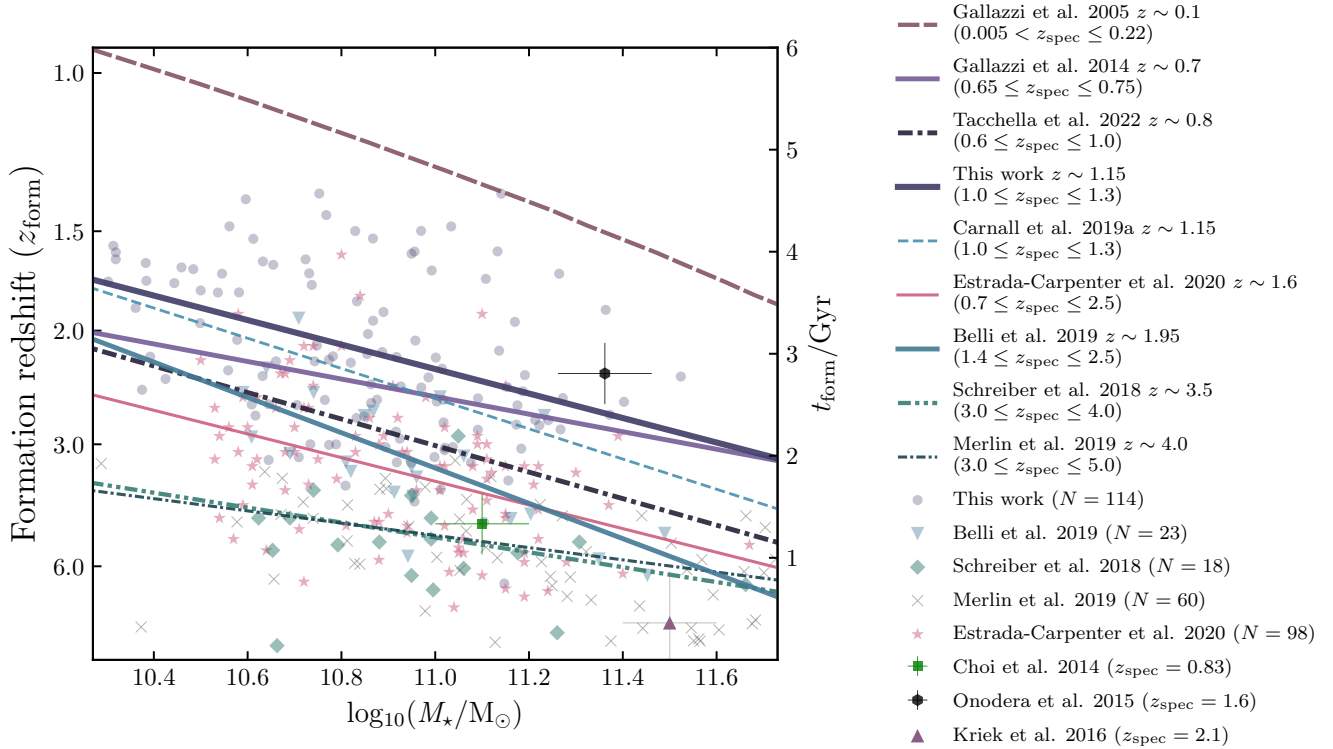


Figure 3. Stellar mass versus formation redshift for massive quiescent galaxies, taken from a range of studies across a wide range in observed redshift. Our sample of VANDELS DR4 quiescent galaxies are shown as circles, and our best-fit line is over-plotted. For some studies that do not report best-fitting relationships between stellar mass and age, we have fitted their results for individual galaxies using the methodology described in Section 4.2. These studies broadly agree on the slope of the relationship, which is found to be consistent at $\simeq 1.5$ Gyr per decade in mass across cosmic history. The normalisation of these relationships does not follow the expected smooth evolution with observed redshift, likely due to methodological differences (see Section 5.1.2).

(2019a), obtaining a result consistent with theirs. We therefore conclude that this offset is a result of our expanded statistical VANDELS DR4 sample, which contains more galaxies that have high stellar masses and lower formation redshifts with respect to the DR2 subset.

We also explore the median relationship between stellar mass and age in our sample by binning our galaxies into equal-width stellar-mass bins of 0.3 dex. This is shown in the right-hand panel of Fig. 2, where the relationship is clear up to stellar masses of $\log_{10}(M_*/M_\odot) \simeq 11.2$. We discuss this relationship in more detail in Section 5.1, making comparisons to relevant literature, which are shown in Fig. 3.

4.3 The oldest galaxy at $z \simeq 1$

From inspection of Fig. 2, it is clear that there is a single galaxy (ID: 111129) which falls significantly below the main stellar mass vs age distribution, with a formation time of $t_{\text{form}} = 0.75^{+0.41}_{-0.29}$ Gyr ($z_{\text{form}} = 7.02^{+3.06}_{-2.07}$), and a quenching time (t_{quench} is defined as the age of the Universe at which the normalised star-formation rate, nSFR, as defined in Carnall et al. 2018, first falls below 0.1) of $t_{\text{quench}} = 1.94^{+0.86}_{-0.67}$ Gyr ($z_{\text{quench}} = 3.23^{+1.41}_{-0.93}$) after the Big Bang, respectively. Given recent reports, based on the first data from JWST, of the assembly of significant numbers of massive galaxies dur-

ing the first billion years (e.g., Labbe et al. 2022), and their subsequent quenching during the second billion years (e.g., Carnall et al. 2022a), this is clearly an object of significant interest.

Upon inspection of the spectrum of this galaxy, and comparison with the best-fit model from our BAGPIPES fitting, we find there is a significant offset between the physical model and observed spectrum in the rest-frame wavelength range 3844 – 3884 Å. This is consistent with the $\lambda = 3860$ Å CN molecular feature (Smith & Norris 1983; Balogh et al. 1999). Motivated by this, we re-inspect the data and best-fit models for our whole sample, finding 10 galaxies in total (including ID: 111129) that clearly demonstrate this feature (see Section 5.3.2). Four example objects from this sub-sample are shown in Fig. 4. We discuss the physical interpretation of this feature in Section 5.3.2.

5 DISCUSSION

In Section 4, we report the relationship between stellar mass and age from full spectral fitting of our mass-complete VANDELS quiescent sample. In this section, we discuss our results, focusing on relationships between age, *UVJ* position, D_n4000 and metallicity evident within our sample. We also

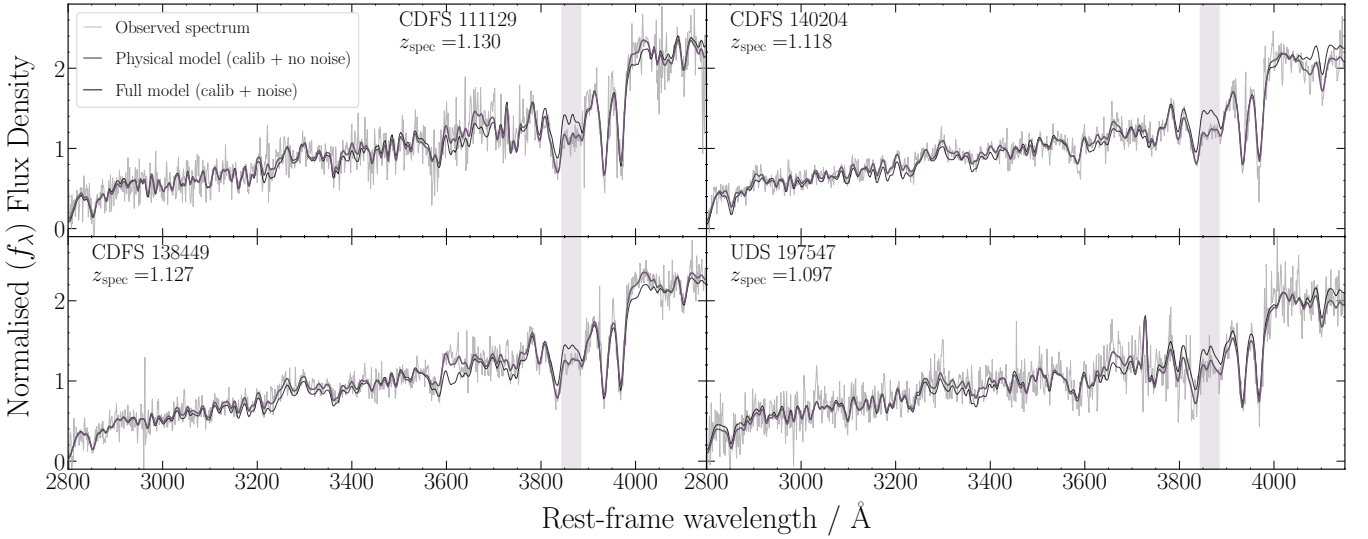


Figure 4. Four galaxies in our sample that display enhanced CN absorption. The VANDELS data are shown in grey. The best-fitting full BAGPIPES models (physical + calibration + noise) are shown in purple. The physical + calibration model, excluding the additive Gaussian process noise model, is shown in black. The shaded wavelength region (3844 – 3884 Å) highlights the CN molecular feature.

explore a subset of galaxies which appear to exhibit spectral features associated with significant α -enhancement.

5.1 The formation times of quiescent galaxies

Over the past decade, extensive research has been conducted into the star-formation histories and ages of quiescent galaxies. This has revealed a sub-population of extremely old galaxies, which formed very early in cosmic history (e.g., Glazebrook et al. 2017; Schreiber et al. 2018; Valentino et al. 2020). These galaxies tend to have higher stellar masses and more compact morphologies than is typical for the quiescent population. In order to constrain the build-up of the quiescent population across cosmic time, and reveal the fate of these oldest, most extreme systems, detailed knowledge of the stellar mass vs stellar age relationship as a function of observed redshift is required. The stellar mass vs stellar age relation presented in Section 4.2 is based on the robust, mass-complete VANDELS spectroscopic sample. In this section, we compare these results with similar studies in the literature, across a broad redshift range.

Our results are placed into the context of recent literature in Fig. 3, which shows results derived by Gallazzi et al. (2005, 2014); Choi et al. (2014); Onodera et al. (2015); Schreiber et al. (2018); Belli et al. (2019); Carnall et al. (2019a); Merlin et al. (2019); Estrada-Carpenter et al. (2020) and Tacchella et al. (2022), with the stellar mass vs age relations derived in various observed redshift ranges over-plotted. For several data-sets shown in the figure, no average relationship between stellar mass and age is calculated by the authors. In these cases, we perform a fit to the individual galaxy masses and ages, using the same method outlined in Section 4.2.

5.1.1 Slopes of the observed relationships

The slope of the stellar mass vs age relationship is intimately connected to the physics of quenching in massive galaxies. We

derive a slope for the VANDELS DR4 sample of $1.20^{+0.28}_{-0.27}$ Gyr per decade in mass. As can be seen from Fig. 3, this is in good agreement with the other literature relationships shown. At the highest redshifts, the sample of Schreiber et al. (2018) at $3.0 < z < 4.0$ displays a slope consistent with our result at $z \simeq 1.1$ to within 2σ . In the local Universe, the results of Gallazzi et al. (2005) also display a very similar slope. This suggests the slope of the stellar mass vs age relationship for massive quiescent galaxies remains broadly constant across cosmic history.

As can be seen from Fig. 3, the results of Belli et al. (2019), who study a sample of 23 massive quiescent galaxies at $1.5 < z < 2.5$ using data from the Keck-MOSFIRE spectrograph, suggest a steeper relation between stellar mass and age. We perform a fit to their galaxies on the stellar mass-age plane, finding a slope of $1.73^{+0.40}_{-0.40}$ Gyr per decade in mass. Whilst this is a steeper slope than our result, it is not strongly in tension, owing to the relatively small samples involved.

In Carnall et al. (2019a) and Tacchella et al. (2022), the authors compare the observed stellar mass vs age relationship with the predictions of cosmological simulations. Carnall et al. (2019a) derive this relationship from snapshots of the $100 h^{-1}$ Mpc box runs of SIMBA (Davé et al. 2019) and ILLUSTRISTNG (Nelson et al. 2018) at $z = 0.1$ and $z = 1.0$. They find that these simulations predict slopes of $\simeq 1.5$ Gyr per decade in mass in the local Universe, but much shallower slopes at $z \sim 1$, with Tacchella et al. (2022) reporting similar findings for IllustrisTNG at $z \sim 0.7$.

Our results are consistent with the predicted slopes of ~ 1.5 Gyr per decade in mass from these two simulations in the local Universe ($z \sim 0.1$). However, our results again suggest that simulations should seek to reproduce the same, steeper stellar mass vs age relationship for massive quiescent galaxies throughout cosmic history.

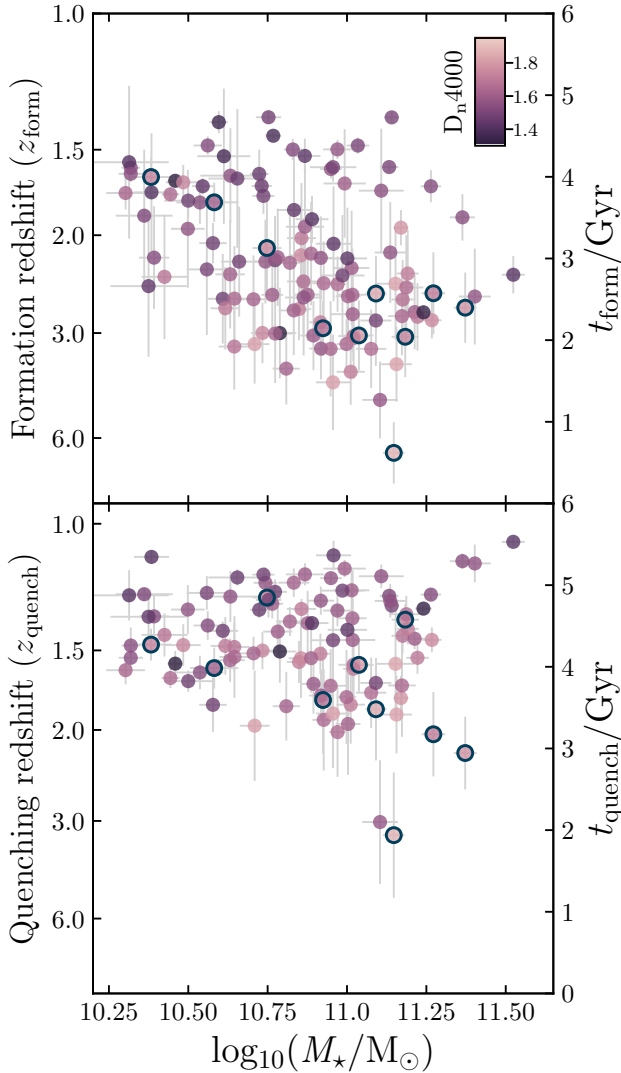


Figure 5. Stellar mass versus formation redshift and quenching redshift (in the top and bottom panels respectively) for our final sample of VANDELs quiescent galaxies. The galaxies are colour-coded by D_n4000 , highlighting that higher values of D_n4000 are observed for galaxies with earlier formation times. Circled galaxies are those that display enhanced CN absorption in their spectra (see Sections 4.3 and 5.3.2).

5.1.2 Normalisations of the observed relationships

The redshift evolution of the average age of quiescent galaxies at fixed stellar mass is influenced primarily by the quenching of new galaxies that join the quiescent population over time (e.g. McLeod et al. 2021). This effect is sometimes known as progenitor bias. The expected evolution of the relationships shown in Fig. 3 due to progenitor bias would be a steady increase in normalisation from high to low redshift. The rate of this decrease in formation redshift with decreasing observed redshift is also highly sensitive to the effects of merger and rejuvenation events.

Unfortunately, this idealised smooth upward evolution with decreasing redshift is not observed in Fig. 3. Whilst studies of galaxy samples at the highest observed redshifts typically

return the highest formation redshifts, and the local-Universe study of Gallazzi et al. (2005) returns the lowest, there is confusion between these extremes. We report later average formation times than all studies targeting higher-redshift galaxy samples; however, both Gallazzi et al. (2014) and Tacchella et al. (2022) also report earlier average formation times than our study, despite analysing samples at lower observed redshifts ($z \simeq 0.7$, as opposed to $z \simeq 1.1$ for our sample).

As has been discussed in several recent works (Tacchella et al. 2022; Carnall et al. 2022b), these differences are likely the result of methodological differences between studies. The two most important of these are different definitions of age (mass-weighted vs light-weighted), and differences between parametric and non-parametric SFH models, the latter of which typically return older stellar ages (Carnall et al. 2019b; Leja et al. 2019a,b). For this reason, a clear understanding of the redshift evolution of the normalisation of this relationship requires a study applying the same methodology to observed samples at a wide range of redshifts.

5.1.3 Number density of the oldest galaxies at $z \simeq 1$

Fig. 5 shows the formation and quenching redshifts of our VANDELs quiescent sample versus stellar mass, in the top and bottom panels, respectively. A significant number of galaxies have formation redshifts of $z_{\text{form}} > 3$, all of which have stellar masses of $\log_{10}(M_*/M_\odot) \geq 10.6$. Only one galaxy has a formation redshift of $z_{\text{form}} > 5$ (see Section 4.3).

Only two galaxies in our sample have quenching redshifts $z_{\text{quench}} > 3$. These objects are of particular interest, given that current simulations seem to under-predict the numbers of galaxies that quenched at these very early times (see Schreiber et al. 2018; Cecchi et al. 2019; Tacchella et al. 2022), possibly due to an additional mechanism capable of causing a rapid early shutdown of star formation, not yet included in simulations. We calculate the number density of galaxies in our VANDELs sample that have $z_{\text{quench}} > 3$, recovering a value of $(1.1 \pm 0.7) \times 10^{-5} \text{ Mpc}^{-3}$. This is consistent with the results of Schreiber et al. (2018), who calculate a number density for quiescent galaxies observed at $3 < z < 4$ of $(1.4 \pm 0.3) \times 10^{-5} \text{ Mpc}^{-3}$. Whilst our sample of such old quiescent galaxies is very small, this preliminary agreement is encouraging, and suggests that neither mergers nor rejuvenation events (both of which could act to reduce the observed ages for such objects) significantly affects this population across the redshift range from $1 < z < 3$.

5.2 The relationship between colour and age

Next we consider the relationship between galaxy stellar age and position on the *UVJ* diagram, performing a stacking analysis of our sample using two bins in rest-frame colour. Following the approach of Whitaker et al. (2013), we divide the sample into two bins on the *UVJ* diagram, separated using the criteria:

$$(U - V) = -1.14 \times (V - J) + 3.10, \quad (2)$$

as illustrated in the inset panel of Fig. 6 by the dot-dashed line. In order to minimise the impact of the correlation between stellar mass and age, we additionally restrict both *UVJ* bins to only include galaxies with $\log_{10}(M_*/M_\odot) \geq 10.6$.

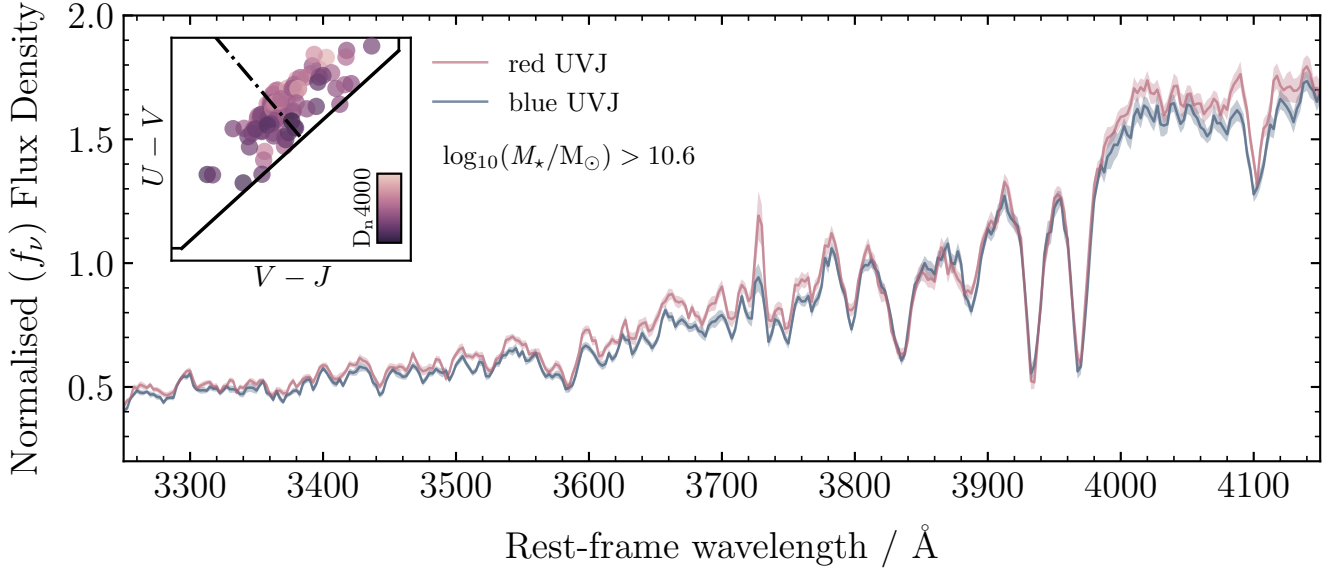


Figure 6. The stacked spectra of our final sample of galaxies (for galaxies with $\log_{10}(M_{\star}/M_{\odot}) \geq 10.6$) in two bins based on their position on the UVJ -diagram. The galaxies are split into blue UVJ and red UVJ populations (see inset) following a method similar to the one adopted by Whitaker et al. (2013). As detailed in the main text, we see an increase in D_{n4000} and median mass-weighted age with increasing UVJ colour (from blue to red).

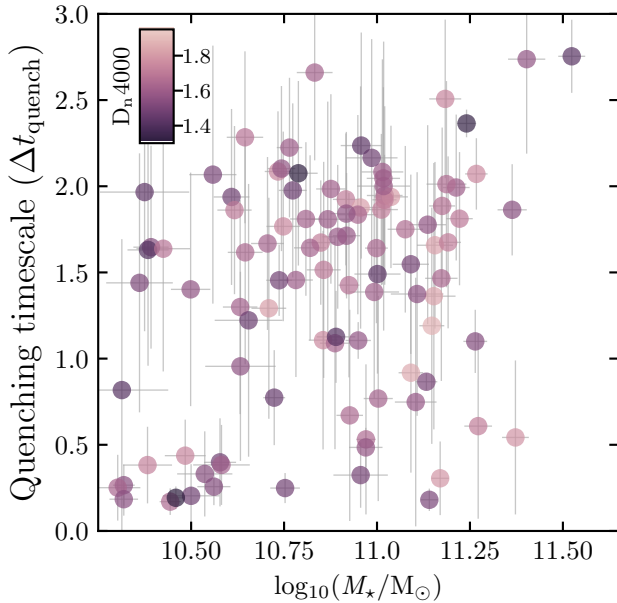


Figure 7. Quenching timescale (Δt_{quench}) versus stellar mass for the full VANDELS quiescent galaxy sample. The value of the D_{n4000} index is shown by the colour bar.

Adopting these criteria produces bins containing similar numbers of objects and comparable median stellar masses; $\log_{10}(M_{\text{med}}/M_{\odot}) = 10.86 \pm 0.03$ and 11.00 ± 0.04 for the blue and red UVJ bins, respectively.

In the main panel of Fig. 6 we show stacked spectra constructed from the objects in each UVJ bin and in Table 2

Table 2. The D_{n4000} values calculated from the stacked spectra shown in Fig. 6. We also report median values in each of the three bins for D_{n4000} and mass-weighted age, where N represents the number of galaxies in each bin.

UVJ position	N	D_{n4000}_{stack}	D_{n4000}_{med}	age / Gyr
Blue UVJ	45	1.57 ± 0.01	1.58 ± 0.03	2.45 ± 0.14
Red UVJ	47	1.66 ± 0.02	1.63 ± 0.04	2.80 ± 0.12

we present D_{n4000} values calculated from the stacked spectra, together with the median D_{n4000} values and stellar ages of the objects in each bin. It is clear from these results that galaxies within the red UVJ bin display larger D_{n4000} values and older stellar ages than their counterparts within the blue UVJ bin, consistent with the expected correlation between age and UVJ colour (e.g., Whitaker et al. 2013; Belli et al. 2019). We note that Whitaker et al. (2013) find ages of $0.9^{+0.2}_{-0.1}$ Gyr and $1.6^{+0.5}_{-0.4}$ Gyr for their blue and red UVJ subsamples, based on stacked grism spectra of quiescent galaxies at $1.4 < z < 2.2$. Within the large uncertainties, this difference of 0.7 ± 0.5 Gyr is fully consistent with the difference of 0.4 ± 0.2 Gyr we find from our analysis.

5.3 Quenching timescales

As discussed in the introduction, recent studies of the star-formation histories of quiescent galaxies point to the existence of multiple quenching channels (e.g., Belli et al. 2019; Carnall et al. 2019a; Tacchella et al. 2022). In general, the star-formation histories we derive for the VANDELS quiescent sample are consistent with this picture, displaying a range of formation and quenching times. However, to investigate

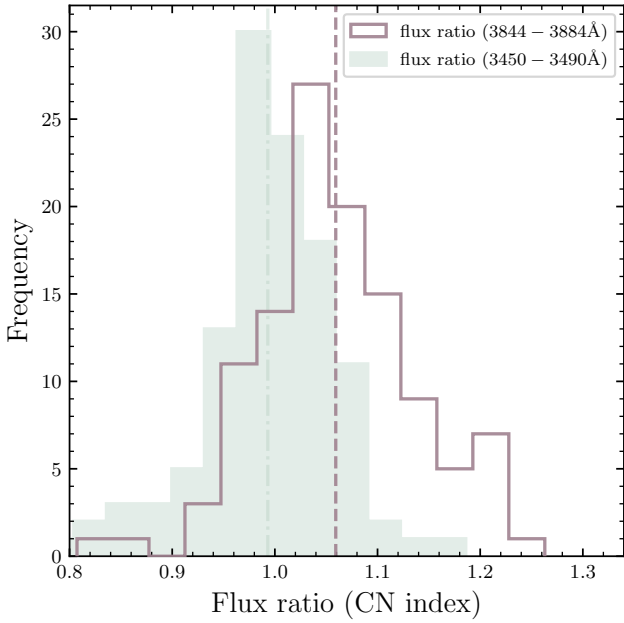


Figure 8. Histogram of the CN index (see main text in Section 5.3.2) calculated within the wavelength range 3844 – 3884 Å (solid line). The green shaded histogram shows the equivalent index calculated on a nearby continuum region free from spectral features. The dashed and dashed-dotted lines correspond to the mean values of the two distributions (see text for discussion).

this issue in more detail it is interesting to define a quenching timescale parameter: Δt_{quench} . In this work, t_{quench} is defined as the age of the Universe at which the normalised star-formation rate (nSFR; see Carnall et al. 2018) falls below 0.1, corresponding to the time after the Big Bang at which a galaxy is labelled as quiescent by our selection criteria. Therefore, the quenching timescale is naturally defined as:

$$\Delta t_{\text{quench}} = t(z_{\text{quench}}) - t(z_{\text{form}}). \quad (3)$$

In Fig. 7, we plot quenching timescale versus stellar mass for the VANDELS quiescent galaxies. It is clear that within our sample there is not a significant correlation between quenching timescale and stellar mass, with some of the highest mass galaxies having quenching timescales of 2 – 3 Gyr, while others quench in significantly less than 1 Gyr. For the full sample we find a mean quenching timescale of $\Delta t_{\text{quench}} = 1.4 \pm 0.1$ Gyr.

5.3.1 The CN molecular feature

In Section 4.3 we highlighted the object (ID: 111129) with the earliest formation time ($t_{\text{form}} = 0.75^{+0.41}_{-0.29}$ Gyr; $z_{\text{form}} = 7.02^{+3.06}_{-2.07}$) in the VANDELS sample. We also noted that this object displayed a significant offset between the BAGPIPES physical model and the observed spectrum around the CN molecular feature at $\lambda = 3860$ Å.

Within the context of constraining the star-formation histories of quiescent galaxies, the CN molecular features are of interest because their strength is known to increase with stellar population age (e.g., Nantais et al. 2013; Choi et al.

2014) and they have also been identified as an indicator of α -enhancement (Thomas et al. 2003).

Historically, the CN molecular features at ~ 3860 Å and ~ 4125 Å have been used to infer Nitrogen abundances in chemically peculiar stars, with the strength of the CN feature at 4125 Å quantified by the Lick indices CN₁ and CN₂. The anomalous strength of the CN absorption seen in globular clusters within the Local Group is attributed to enhanced Nitrogen abundance, with many studies finding anti-correlations between CN and CH (which traces the carbon abundance) (e.g., Smith & Norris 1983; Burstein et al. 1984; Smith 1987). Moreover, fitting the Lick indices of 20 extragalactic globular clusters with SSP models, Proctor et al. (2004) highlight the poor fits to CN indices caused by enhanced Nitrogen abundance.

Studying a sample of elliptical galaxies and globular clusters, Thomas et al. (2003) find that a Nitrogen abundance enhancement of a factor of $\simeq 3$ with respect to other alpha elements is required to reproduce the observed CN₁ and CN₂ indices. Interestingly, this study also shows that CN absorption strength increases with α -enhancement at fixed total metallicity, mainly due to an anti-correlation with iron abundance. As a result, the strength of the CN absorption features could provide important information on the typical star-formation timescales of high-redshift quiescent galaxies (e.g., Thomas et al. 2002, 2010).

Recent studies of passive galaxies at $z \simeq 1$ show no clear evidence for evolution in the level of α -enhancement over the last $\simeq 8$ Gyr, typically finding values of $[\text{Mg}/\text{Fe}] \simeq 0.2$ (Kriek et al. 2019; Carnall et al. 2022b), consistent with observations in the local Universe (Conroy et al. 2014). Although some studies have identified a small number of objects with significantly higher α -enhancement (e.g., Kriek et al. 2016; Jafariyazani et al. 2020), this has been attributed to their extreme stellar masses ($\log_{10}(M_{\star}/M_{\odot}) \geq 11.5$), consistent with our current understanding that more-massive early-type galaxies are more α -enhanced than their less-massive counterparts, due to their shorter formation timescales.

5.3.2 Selection of the CN enhanced sub-sample

In order to investigate the prevalence of the CN molecular feature in our VANDELS sample, we now proceed to calculate a CN index. During the spectral fitting with BAGPIPES, once the model has been calibrated for systematic effects by our multiplicative polynomial model, any remaining mismatch to the data around the CN feature is accounted for by the Gaussian process correlated noise model. Therefore, within the wavelength range 3844 – 3884 Å, we define the CN index as the ratio of the median flux in the data and the median flux of the BAGPIPES physical model multiplied by this polynomial but excluding the Gaussian process noise model. This is the ratio of the black model and grey data in Fig. 4 within the shaded wavelength range.

In Fig. 8 we show a histogram of this CN index for our final VANDELS quiescent galaxy sample. It can be seen that the distribution of the CN index has a median value of 1.05, offset from unity, and shows a tail towards higher values. For comparison, the green shaded histogram shows the equivalent index calculated within a featureless continuum region shortward of the CN feature, from 3450 – 3490 Å. As expected, the distribution of index values in this comparison spectral

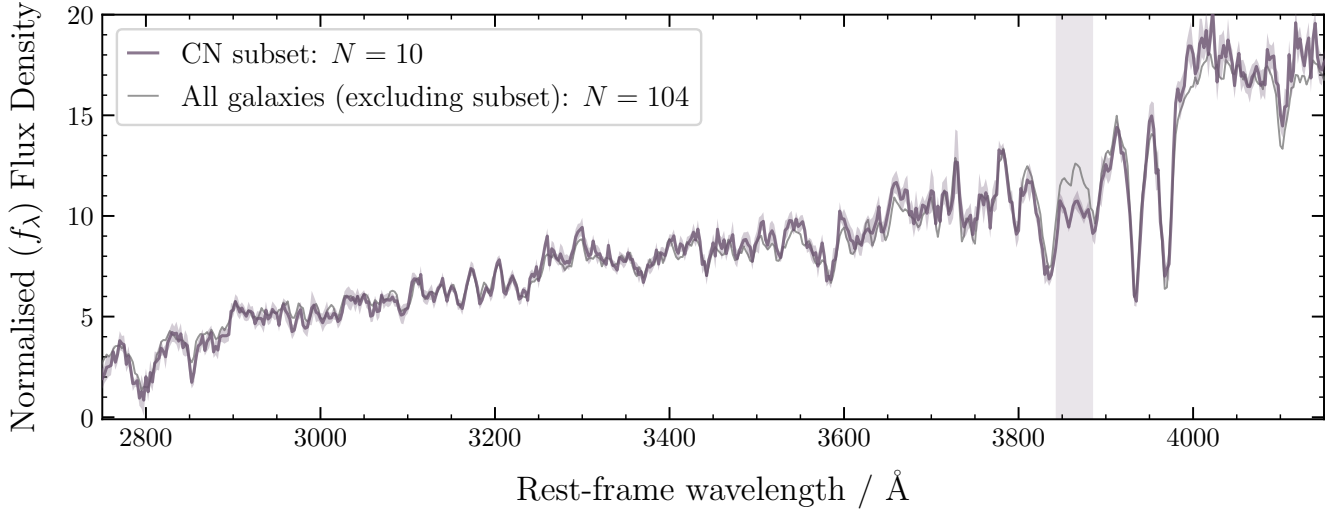


Figure 9. Stacked spectrum of the ten galaxies in our CN enhanced sub-sample compared to the stacked spectrum of the rest of the galaxies in the full sample (in grey, $N=104$). The enhanced absorption within the rest-frame wavelength range of $3844 - 3884 \text{ \AA}$ is clear.

region is symmetric and centred on unity. This corresponds to a zero average correction being made by our Gaussian process correlated noise model over this comparison wavelength range, whereas on average a negative Gaussian process correction is required to explain the data within our CN index wavelength range.

To define the sub-sample of objects that display enhanced CN absorption, we initially select the 14 objects with a CN index greater than 1.15. Visual inspection of these objects confirms that 10 unambiguously display the CN feature, with the remaining four having spectra that are too noisy in the relevant wavelength range to return robust CN index measurements. We additionally re-inspect our entire sample (an additional 100 objects), but find no further objects that unambiguously display this feature. As a result, we consider the 10 unambiguous objects with a CN index greater than 1.15 as our final CN enhanced sub-sample.

5.3.3 Physical properties of the CN enhanced sub-sample

In Fig. 9 we show a stacked spectrum of the CN enhanced sub-sample and compare it to a stacked spectrum of the remaining galaxies in the full VANDELS quiescent galaxy sample. This figure clearly illustrates the enhanced absorption within the CN index wavelength range, which, as discussed in Section 5.3.2, has been linked to older stellar populations and α -enhancement. Relevant physical parameters returned by our BAGPIPES fitting to the 10 objects within the CN enhanced sub-sample are displayed in Table 3.

As discussed above, multiple previous studies at low redshift have associated enhanced CN absorption with old stellar populations. For our VANDELS sample of quiescent galaxies at $z \simeq 1.1$, the median mass-weighted age of the CN enhanced sub-sample is $2.81 \pm 0.34 \text{ Gyr}$, compared to $2.48 \pm 0.10 \text{ Gyr}$ for the main body of the VANDELS sample. It is clear that the trend for strong CN absorption to be related to increased stellar population age is present in our $z \simeq 1.1$ sample, although the difference in median ages

is not statistically significant. As would be expected, the CN enhanced sub-sample also has a larger median stellar mass ($\log_{10}(M_*/M_\odot) = 11.06 \pm 0.12$) compared with the rest of the sample ($\log_{10}(M_*/M_\odot) = 10.86 \pm 0.03$) but again, the difference is not strongly significant. The CN sub-sample does have a significantly higher median value of D_n4000 (1.73 ± 0.03 compared to 1.56 ± 0.01), but unfortunately this is somewhat inevitable, given that the CN index lies within the blue continuum band of the D_n4000 index.

Overall, it appears that the ten objects comprising the CN enhanced sub-sample are consistent with being older and higher mass than the average member of our $z \simeq 1.1$ sample of quiescent galaxies, although small number statistics prevents us from drawing any firm conclusions.

5.3.4 Star-formation histories of the CN enhanced sub-sample

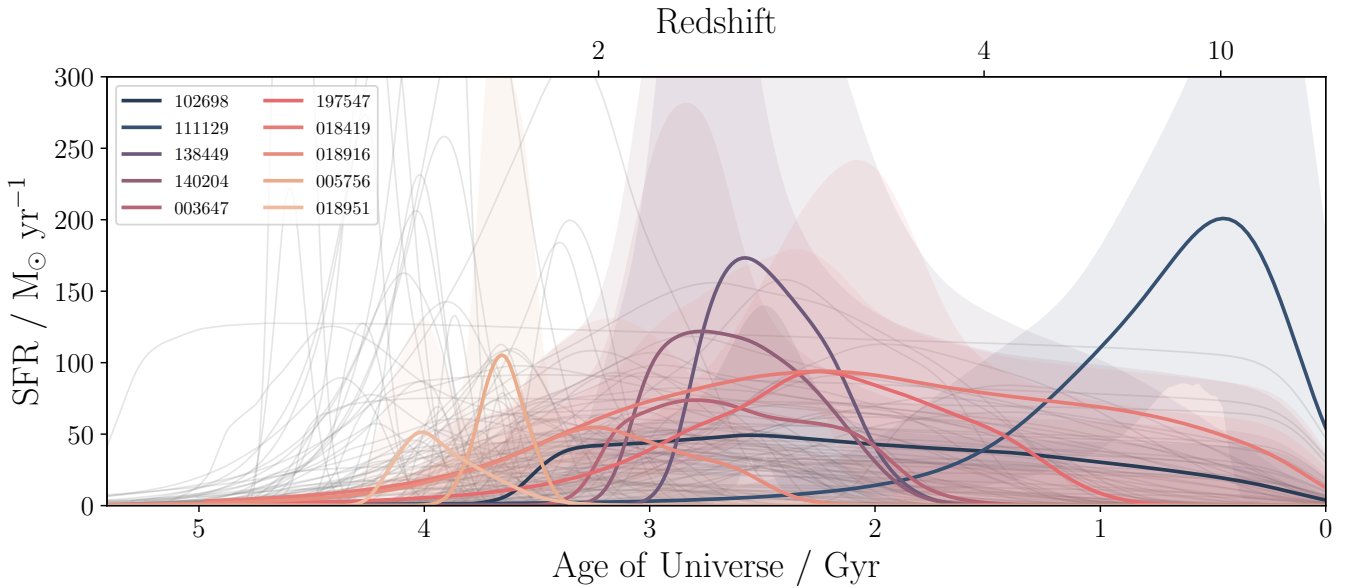
In Fig. 10 we show the posterior star-formation histories of the CN enhanced sub-sample returned by BAGPIPES. With the exception of a single galaxy (ID: 111129), which appears to be an isolated case of a very early formation and quenching time (see Section 4.3), the majority of the CN enhanced sub-sample have formation redshifts of $z_{\text{form}} = 2 - 3$ and display relatively short quenching timescales.

Given that α -enhancement should be associated with short star-formation timescales, it is interesting to compare the star-formation timescales of the CN enhanced sub-sample with those of the sample as a whole. Defining the star-formation timescale as the width of the posterior SFH between the 16th and 84th percentiles, we find the CN sub-sample to have a median timescale of $1.15 \pm 0.34 \text{ Gyr}$, compared to a median timescale of $1.52 \pm 0.10 \text{ Gyr}$ for the rest of the sample. Although the difference in star-formation timescale of $\simeq 400 \text{ Myr}$ is clearly not statistically significant, it is consistent with enhanced CN absorption being connected with α -enhancement.

Finally, it is interesting to note that the two youngest mem-

Table 3. Relevant physical properties of the galaxies within the CN enhanced sub-sample (ordered by t_{form}).

ID	z_{spec}	Z_{\star}/Z_{\odot}	$\log_{10}(M_{\star}/M_{\odot})$	$t_{\text{form}}/\text{Gyr}$	$t_{\text{quench}}/\text{Gyr}$	D_n4000	$f_{\text{mod}}/f_{\text{data}}$
018951	1.093	$0.66^{+0.10}_{-0.06}$	$10.38^{+0.08}_{-0.05}$	$3.89^{+0.17}_{-0.27}$	$4.27^{+0.22}_{-0.17}$	1.72 ± 0.01	1.16
005756	1.251	$0.55^{+0.08}_{-0.06}$	$10.58^{+0.04}_{-0.11}$	$3.60^{+0.35}_{-0.10}$	$3.98^{+0.24}_{-0.26}$	1.60 ± 0.03	1.20
018916	1.094	$0.68^{+0.11}_{-0.09}$	$10.75^{+0.05}_{-0.04}$	$3.08^{+0.33}_{-0.73}$	$4.85^{+0.19}_{-0.13}$	1.74 ± 0.01	1.15
140204	1.118	$0.54^{+0.09}_{-0.08}$	$11.27^{+0.03}_{-0.05}$	$2.57^{+0.34}_{-0.59}$	$3.17^{+0.60}_{-0.43}$	1.70 ± 0.01	1.17
003647	1.097	$0.65^{+0.12}_{-0.07}$	$11.09^{+0.03}_{-0.04}$	$2.56^{+0.38}_{-0.47}$	$3.48^{+0.66}_{-0.59}$	1.84 ± 0.01	1.19
138449	1.127	$0.62^{+0.07}_{-0.05}$	$11.37^{+0.04}_{-0.04}$	$2.40^{+0.34}_{-0.46}$	$2.94^{+0.48}_{-0.42}$	1.77 ± 0.01	1.17
102698	1.221	$0.58^{+0.07}_{-0.05}$	$10.92^{+0.03}_{-0.03}$	$2.17^{+0.38}_{-0.25}$	$3.59^{+0.38}_{-0.94}$	1.67 ± 0.01	1.17
197547	1.096	$0.73^{+0.10}_{-0.08}$	$11.04^{+0.04}_{-0.05}$	$2.09^{+0.37}_{-0.42}$	$4.02^{+0.30}_{-0.35}$	1.80 ± 0.01	1.18
018419	1.221	$0.96^{+0.21}_{-0.16}$	$11.18^{+0.04}_{-0.05}$	$2.07^{+0.63}_{-0.29}$	$4.58^{+0.17}_{-0.22}$	1.73 ± 0.01	1.21
111129	1.130	$0.80^{+0.10}_{-0.10}$	$11.15^{+0.04}_{-0.03}$	$0.75^{+0.41}_{-0.29}$	$1.94^{+0.86}_{-0.67}$	1.86 ± 0.01	1.21

**Figure 10.** Star-formation histories for the 10 quiescent galaxies in our final sample which show enhanced CN absorption. The grey lines in the background are the SFHs for the rest of the galaxies in the sample ($N = 104$).

bers of the CN enhanced sub-sample (ID: 018951 and ID: 005756) have stellar masses that are in the lowest quartile of the full VANDELS sample. This combination of relative youth and low stellar mass would not identify them as obvious candidates to display enhanced CN absorption. However, as can be seen from Fig. 10, both objects have very short star-formation timescales, consistent with them both being α -enhanced.

In order to gain further insight into the physical properties and SFHs of the CN enhanced sub-sample, and the $z \simeq 1.1$ VANDELS sample as a whole, it is clear that near-IR spectroscopy is required. In addition to placing significantly tighter constraints on the SFHs and overall metallicities (Carnall et al. 2022b), such rest-frame optical spectroscopy would allow access to several indices sensitive to α -enhancement and Nitrogen abundance (e.g. CN₁, CN₂, Ca4227 and Mg_b). Over the next few years, the MOONS spectrograph (Cirasuolo et al. 2020) will be able to provide the necessary near-

IR spectroscopy for large samples of passive galaxies out to $z \simeq 2.5$, while NIRSpect on *JWST* can in principle provide access to the full set of Lick indices out to $z \simeq 6.5$.

6 CONCLUSIONS

In this paper, we have explored the relationships between stellar mass, age, star-formation history and quenching timescales for a robust spectroscopic sample of quiescent galaxies at $1.0 < z < 1.3$. Our main results and conclusions can be summarised as follows:

- (i) We derive significantly improved constraints on the relationship between stellar population age and stellar mass for quiescent galaxies at $z \simeq 1.1$. From our full VANDELS sample we derive an age-mass relation which has a slope of $1.20^{+0.28}_{-0.27}$ Gyr per decade in stellar mass.

- (ii) Comparing to previous studies in the literature, we find good agreement on the slope of the age-mass relation for quiescent galaxies from the local Universe out to $z \simeq 4$. The observed slope is in good agreement with the prediction from simulations at $z \simeq 0$, but significantly steeper than simulations predict at $z \geq 1$.
- (iii) The results of our spectro-photometric fitting predict that the number density of already quenched galaxies at $z \geq 3$ with stellar masses $\log_{10}(M_*/M_\odot) \geq 10.6$ is $(1.1 \pm 0.7) \times 10^{-5} \text{ Mpc}^{-3}$. Although subject to a large uncertainty due to small-number statistics, this estimate is in good agreement with the latest measurements at $3 < z < 4$. The implication is that rejuvenation or merger events are not playing a major role in modulating the number density of the oldest massive quiescent galaxies within the redshift interval $1 < z < 3$.
- (iv) We confirm previously reported results that quiescent galaxies with redder *UVJ* colours are systematically older than their bluer counterparts, finding an off-set of 0.4 ± 0.2 Gyr in the median age of mass-matched samples.
- (v) The VANDELS sample of $z \simeq 1.1$ quiescent galaxies displays a wide range of formation and quenching redshifts. We find that the mean star-formation timescale is 1.5 ± 0.1 Gyr, where the timescale is defined as the width of the posterior SFH between the 16th and 84th percentiles. We find that the mean quenching timescale is 1.4 ± 0.1 Gyr, where $\Delta t_{\text{quench}} = t(z_{\text{quench}}) - t(z_{\text{form}})$. The oldest galaxy within the VANDELS sample (ID: 111129) has $z_{\text{form}} = 7.02^{+3.06}_{-2.07}$ and $z_{\text{quench}} = 3.23^{+1.41}_{-0.93}$.
- (vi) We identify a small sub-sample of galaxies which exhibit enhanced absorption in the CN molecular feature at $\lambda = 3860 \text{ \AA}$, which has previously been identified to correlate with old stellar population age and α -enhancement. This CN enhanced sub-sample displays older ages, higher stellar masses and shorter star-formation timescales than the rest of the sample, consistent with expectations for α -enhancement. However, due to small number statistics, none of the differences between the CN sub-sample and the full sample are statistically significant, making it difficult to draw firm conclusions from this dataset alone.

ACKNOWLEDGEMENTS

M. L. Hamadouche, R. Begley, and C. T. Donnan acknowledge the support of the UK Science and Technology Facilities Council. A. C. Carnall acknowledges the support of the Leverhulme Trust. F. Cullen and T. M. Stanton acknowledge support from a UKRI Frontier Research Guarantee Grant (PI Cullen; grant reference EP/X021025/1). Based on observations made with ESO Telescopes at the La Silla or Paranal Observatories under programme ID(s) 194.A-2003(E-Q) (The VANDELS ESO Public Spectroscopic Survey). Based on data products from observations made with ESO Telescopes at the La Silla Paranal Observatory under ESO programme ID 179.A-2005 and on data products produced by TERAPIX and the Cambridge Astronomy Survey Unit on behalf of the UltraVISTA consortium. This research made use of Astropy, a community-developed core Python package for Astronomy (Astropy Collaboration et al. 2013, 2018).

DATA AVAILABILITY

The VANDELS survey is a European Southern Observatory Public Spectroscopic Survey. The full spectroscopic dataset, together with the complementary photometric information and derived quantities are available from <http://vandels.inaf.it>, as well as from the ESO archive <https://www.eso.org/qi/>.

REFERENCES

- Abraham R. G., et al., 2004, *AJ*, **127**, 2455
- Akins H. B., Narayanan D., Whitaker K. E., Davé R., Lower S., Bezanson R., Feldmann R., Kriek M., 2022, *ApJ*, **929**, 94
- Asplund M., Grevesse N., Sauval A. J., Scott P., 2009, *ARA&A*, **47**, 481
- Astropy Collaboration et al., 2013, *A&A*, **558**, A33
- Astropy Collaboration et al., 2018, *AJ*, **156**, 123
- Baldry I. K., Glazebrook K., Brinkmann J., Ivezić Ž., Lupton R. H., Nichol R. C., Szalay A. S., 2004, *ApJ*, **600**, 681
- Baldry I. K., et al., 2012, *MNRAS*, **421**, 621
- Balogh M. L., Morris S. L., Yee H. K. C., Carlberg R. G., Ellingson E., 1999, *ApJ*, **527**, 54
- Belli S., Newman A. B., Ellis R. S., 2019, *The Astrophysical Journal*, **874**, 17
- Beverage A. G., Kriek M., Conroy C., Bezanson R., Franx M., van der Wel A., 2021, arXiv e-prints, p. [arXiv:2105.12750](https://arxiv.org/abs/2105.12750)
- Bonzini M., Padovani P., Mainieri V., Kellermann K. I., Miller N., Rosati P., Tozzi P., Vattakunnel S., 2013, *MNRAS*, **436**, 3759
- Brinchmann J., Charlot S., White S. D. M., Tremonti C., Kauffmann G., Heckman T., Brinkmann J., 2004, *MNRAS*, **351**, 1151
- Bruzual G., 1983, *ApJ*, **273**, 105
- Bruzual G., Charlot S., 2003, *MNRAS*, **344**, 1000
- Buchner J., 2016, *Statistics and Computing*, **26**, 383
- Buchner J., 2019, *PASP*, **131**, 108005
- Buchner J., 2021, *The Journal of Open Source Software*, **6**, 3001
- Burstein D., Faber S. M., Gaskell C. M., Krumm N., 1984, *ApJ*, **287**, 586
- Byler N., Dalcanton J. J., Conroy C., Johnson B. D., 2017, *ApJ*, **840**, 44
- Calzetti D., Armus L., Bohlin R. C., Kinney A. L., Koornneef J., Storchi-Bergmann T., 2000, *ApJ*, **533**, 682
- Cappellari M., 2017, *MNRAS*, **466**, 798
- Carnall A. C., 2017, arXiv e-prints, p. [arXiv:1705.05165](https://arxiv.org/abs/1705.05165)
- Carnall A. C., McLure R. J., Dunlop J. S., Davé R., 2018, *MNRAS*, **480**, 4379
- Carnall A. C., et al., 2019a, *MNRAS*, **490**, 417
- Carnall A. C., Leja J., Johnson B. D., McLure R. J., Dunlop J. S., Conroy C., 2019b, *The Astrophysical Journal*, **873**, 44
- Carnall A. C., et al., 2020, *MNRAS*, **496**, 695
- Carnall A. C., et al., 2022a, arXiv e-prints, p. [arXiv:2208.00986](https://arxiv.org/abs/2208.00986)
- Carnall A. C., et al., 2022b, *ApJ*, **929**, 131
- Cecchi R., Bolzonella M., Cimatti A., Girelli G., 2019, *ApJ*, **880**, L14
- Chevallard J., Charlot S., 2016, *MNRAS*, **462**, 1415
- Choi J., Conroy C., Moustakas J., Graves G. J., Holden B. P., Brodwin M., Brown M. J. I., van Dokkum P. G., 2014, *ApJ*, **792**, 95
- Choi E., Somerville R. S., Ostriker J. P., Naab T., Hirschmann M., 2018, *The Astrophysical Journal*, **866**, 91
- Cimatti A., et al., 2002, *A&A*, **381**, L68
- Cimatti A., Nipoti C., Cassata P., 2012, *MNRAS*, **422**, L62
- Cirasuolo M., et al., 2020, *The Messenger*, **180**, 10
- Conroy C., Graves G. J., van Dokkum P. G., 2014, *ApJ*, **780**, 33
- Cowie L. L., Songaila A., Hu E. M., Cohen J. G., 1996, *AJ*, **112**, 839

- Croton D. J., et al., 2006, *MNRAS*, **365**, 11
- Davé R., Rafieferantsoa M. H., Thompson R. J., 2017, *MNRAS*, **471**, 1671
- Davé R., Anglés-Alcázar D., Narayanan D., Li Q., Rafieferantsoa M. H., Appleby S., 2019, *MNRAS*, **486**, 2827
- Davidzon I., et al., 2017, *A&A*, **605**, A70
- Dekel A., Birnboim Y., 2006, *MNRAS*, **368**, 2
- Estrada-Carpenter V., et al., 2020, *ApJ*, **898**, 171
- Ferland G. J., et al., 2017, *Rev. Mex. Astron. Astrofis.*, **53**, 385
- Fontana A., et al., 2006, *A&A*, **459**, 745
- Fontanot F., De Lucia G., Monaco P., Somerville R. S., Santini P., 2009, *MNRAS*, **397**, 1776
- Gabor J. M., Davé R., 2012, *MNRAS*, **427**, 1816
- Gabor J. M., Davé R., Oppenheimer B. D., Finlator K., 2011, *MNRAS*, **417**, 2676
- Galametz A., et al., 2013, *ApJS*, **206**, 10
- Gallazzi A., Charlot S., Brinchmann J., White S. D. M., Tremonti C. A., 2005, *MNRAS*, **362**, 41
- Gallazzi A., Bell E. F., Zibetti S., Brinchmann J., Kelson D. D., 2014, *ApJ*, **788**, 72
- Garilli B., et al., 2021, *A&A*, **647**, A150
- Glazebrook K., et al., 2017, *Nature*, **544**, 71
- Guo Y., et al., 2013, *ApJS*, **207**, 24
- Hamadouche M. L., et al., 2022, *MNRAS*, **512**, 1262
- Hopkins P. F., et al., 2010, *ApJ*, **724**, 915
- Jafariyazani M., Newman A. B., Mobasher B., Belli S., Ellis R. S., Patel S. G., 2020, *ApJ*, **897**, L42
- Johnson B. D., Leja J., Conroy C., Speagle J. S., 2021, *ApJS*, **254**, 22
- Kauffmann G., et al., 2003, *MNRAS*, **341**, 33
- Kocevski D. D., et al., 2018, *ApJS*, **236**, 48
- Kriek M., et al., 2016, *Nature*, **540**, 248
- Kriek M., et al., 2019, *ApJ*, **880**, L31
- Kroupa P., 2001, *MNRAS*, **322**, 231
- Labbe I., et al., 2022, arXiv e-prints, p. arXiv:2207.12446
- Le Fèvre O., et al., 2004, *A&A*, **428**, 1043
- Le Fèvre O., et al., 2013, *A&A*, **559**, A14
- Leja J., Carnall A. C., Johnson B. D., Conroy C., Speagle J. S., 2019a, *ApJ*, **876**, 3
- Leja J., et al., 2019b, *ApJ*, **877**, 140
- Luo B., et al., 2017, VizieR Online Data Catalog, p. J/ApJS/228/2
- McLeod D. J., McLure R. J., Dunlop J. S., Cullen F., Carnall A. C., Duncan K., 2021, *MNRAS*, **503**, 4413
- McLure R. J., et al., 2013, *MNRAS*, **428**, 1088
- McLure R. J., et al., 2018, *MNRAS*, **479**, 25
- Merlin E., et al., 2019, *MNRAS*, **490**, 3309
- Moresco M., et al., 2010, *A&A*, **524**, A67
- Moresco M., Jimenez R., Cimatti A., Pozzetti L., 2011, *J. Cosmology Astropart. Phys.*, **2011**, 045
- Moresco M., et al., 2016, *J. Cosmology Astropart. Phys.*, **2016**, 014
- Mowla L. A., et al., 2019, *ApJ*, **880**, 57
- Muzzin A., et al., 2013, *ApJS*, **206**, 8
- Nantais J. B., Rettura A., Lidman C., Demarco R., Gobat R., Rosati P., Jee M. J., 2013, *A&A*, **556**, A112
- Nelson D., et al., 2018, *MNRAS*, **475**, 624
- Onodera M., et al., 2015, *ApJ*, **808**, 161
- Ownsworth J. R., Conselice C. J., Mortlock A., Hartley W. G., Almaini O., Duncan K., Mundy C. J., 2014, *MNRAS*, **445**, 2198
- Pacifici C., et al., 2016, *ApJ*, **832**, 79
- Peng C. Y., Ho L. C., Impey C. D., Rix H.-W., 2002, *AJ*, **124**, 266
- Peng Y.-j., et al., 2010, *ApJ*, **721**, 193
- Peng Y., Maiolino R., Cochrane R., 2015, *Nature*, **521**, 192
- Pentericci L., et al., 2018, *A&A*, **616**, A174
- Proctor R. N., Forbes D. A., Beasley M. A., 2004, *MNRAS*, **355**, 1327
- Salim S., Boquien M., Lee J. C., 2018, *The Astrophysical Journal*, **859**, 11
- Schawinski K., et al., 2014, *MNRAS*, **440**, 889
- Schreiber C., Elbaz D., Pannella M., Ciesla L., Wang T., Koeke-moer A., Rafelski M., Daddi E., 2016, *A&A*, **589**, A35
- Schreiber C., et al., 2018, *A&A*, **618**, A85
- Shen S., Mo H. J., White S. D. M., Blanton M. R., Kauffmann G., Voges W., Brinkmann J., Csabai I., 2003, *MNRAS*, **343**, 978
- Simpson C., et al., 2006, *MNRAS*, **372**, 741
- Smith G. H., 1987, *PASP*, **99**, 67
- Smith G. H., Norris J., 1983, *ApJ*, **264**, 215
- Somerville R. S., Davé R., 2015, *Annual Review of Astronomy and Astrophysics*, **53**, 51–113
- Strateva I., et al., 2001, *AJ*, **122**, 1861
- Tacchella S., et al., 2022, *ApJ*, **926**, 134
- Thomas D., Maraston C., Bender R., 2002, *Ap&SS*, **281**, 371
- Thomas D., Maraston C., Bender R., 2003, *MNRAS*, **339**, 897
- Thomas D., Maraston C., Bender R., 2005a, Highlights of Astronomy, **13**, 189
- Thomas D., Maraston C., Bender R., Mendes de Oliveira C., 2005b, *ApJ*, **621**, 673
- Thomas D., Maraston C., Schawinski K., Sarzi M., Silk J., 2010, *MNRAS*, **404**, 1775
- Trujillo I., et al., 2006, *ApJ*, **650**, 18
- Trujillo I., Ferreras I., de La Rosa I. G., 2011, *MNRAS*, **415**, 3903
- Trussler J., Maiolino R., Maraston C., Peng Y., Thomas D., Goddard D., Lian J., 2020, *MNRAS*, **491**, 5406
- Valentino F., et al., 2020, *ApJ*, **889**, 93
- Whitaker K. E., et al., 2013, *ApJ*, **770**, L39
- Wild V., Almaini O., Dunlop J., Simpson C., Rowlands K., Bowler R., Maltby D., McLure R., 2016, *MNRAS*, **463**, 832
- Williams R. J., Quadri R. F., Franx M., van Dokkum P., Labbé I., 2009, *ApJ*, **691**, 1879
- Wu P.-F., et al., 2018, *ApJ*, **868**, 37
- Wu P.-F., et al., 2021, arXiv e-prints, p. arXiv:2108.10455
- York D. G., et al., 2000, *The Astronomical Journal*, **120**, 1579–1587
- van der Wel A., et al., 2014, *ApJ*, **788**, 28
- van der Wel A., et al., 2016, *ApJS*, **223**, 29

This paper has been typeset from a \LaTeX file prepared by the author.